



Cite this: *Nanoscale*, 2018, **10**, 22549

Metallic MoS₂ nanosheets: multifunctional electrocatalyst for the ORR, OER and Li–O₂ batteries†

Zoya Sadighi,^a Jiapeng Liu,^a Ling Zhao,^a Francesco Ciucci^{a,b} and Jang-Kyo Kim^{a*}

Lithium–oxygen batteries (LOBs) possess the highest theoretical specific density among all types of lithium batteries, making them ideal candidates to replace the current Li ion batteries for next-generation electric vehicle applications. However, designing highly active catalysts with high electronic conductivities to kinetically accelerate the sluggish oxygen reduction/evolution reactions (ORR/OER) is still a big challenge. This work was dedicated to developing two-dimensional (2D) trigonal phase MoS₂ (1T-MoS₂) nanosheets as a highly active electrocatalyst for LOBs for the first time. Metallic 1T-MoS₂ prepared *via in situ* liquid-redox intercalation and exfoliation was hybridized with functionalized carbon nanotubes (CNTs) to form freestanding, binder-free oxygen electrodes. The 1T-MoS₂/CNT electrode exhibited excellent electrochemical performances with a high reversible capacity of 500 mA h g⁻¹ at a current density of 200 mA g⁻¹ for more than 100 cycles owing to the catalytically active surfaces of 1T-MoS₂ accessible by Li⁺ ions and O₂. Density functional theory (DFT) calculations identified the catalytically active basal planes in 1T-MoS₂ during the ORR as well as the initial ORR path during LOB cycles. The results based on the rotational ring disk electrode (RRDE) experiments also supported the findings from the DFT calculations, where the 1T-MoS₂ basal planes are active for both the ORR and OER, not the semiconducting hexagonal MoS₂ (2H-MoS₂) whose edges are only electrocatalytically active. This study sheds light on the use of metallic 1T-MoS₂ as a multifunctional oxygen electrocatalyst for LOB applications with enhanced ORR and OER activities.

Received 31st August 2018,
Accepted 14th November 2018

DOI: 10.1039/c8nr07106c

rs.c.li/nanoscale

Introduction

Considering the increasing environmental concerns, there is an urgent need to develop clean and renewable energy sources, such as sunlight, wind, rain and waves. Utilization of these energy sources necessitates the development of efficient energy conversion and storage technologies, such as fuel cells, water splitting devices,^{1,2} and rechargeable Li-ion (LIB) and metal–air batteries.³ Li–O₂ batteries (LOB) with the highest theoretical specific energy (3500 W h kg⁻¹) among all types of

batteries are considered a promising alternative to the current Li-ion batteries for use in electric vehicles. However, the practical energy storage capability of LOBs is still very uncertain due to many unknown and problematic factors, such as large polarization, poor cyclic stability and low coulombic efficiencies.^{4,5} One of the most important issues hindering the commercialization of LOBs is the lack of high-performance catalysts to enhance the kinetics of the oxygen reduction/evolution reactions (ORR/OER).⁵

Considering the abovementioned issues, various materials have been explored as catalysts for oxygen electrodes, such as nanocarbons,^{6,7} precious metals,^{8,9} transition metal-oxides^{10,11} and -sulfides,^{12,13} and metal–organic framework-based structures.^{2,14} Furthermore, different structures including nanoparticles (NPs),^{8,15} nanotubes,^{16,17} nanofibers,¹⁰ and two-^{9,18} or three-dimensional¹⁹ (2D or 3D) morphologies have been designed. Among them, layered 2D materials have shown exciting characteristics, including novel electronic properties ranging from insulator to metallic and the ability to electrochemically intercalate Li⁺ ions to form a nanosheet structure with large surface areas and enhanced ionic transport.^{20,21} Although graphene is a well-known 2D material with very high electrical conductivity, it is chemically inert and needs

^aDepartment of Mechanical and Aerospace Engineering, The Hong Kong University of Science and Technology, Clear Water Bay, Hong Kong. E-mail: mejkkm@ust.hk

^bDepartment of Chemical and Biomolecular Engineering, The Hong Kong University of Science and Technology, Clear Water Bay, Hong Kong

† Electronic supplementary information (ESI) available: Preparation of electrode materials, characterizations, electrochemical measurements, DFT calculations, Li diffusion coefficient calculations, XRD and XPS spectra of CNTs, SEM images and EDX analysis, *ex situ* XPS spectra during cycles, *ex situ* XRD spectra and HRTEM images of 1T-MoS₂/CNT upon cycles, EIS spectra, CV curves, XPS spectra for the edge-oxidized 1T-MoS₂, impedance parameters, electrical conductivities, carrier concentrations and lithium diffusion coefficients, adsorption energies of O₂ on basal planes and Mo edges, and Li and Li_xO_y on basal planes of 2H- and 1T-MoS₂. See DOI: 10.1039/c8nr07106c

functionalization with other molecules, which may adversely affect some desired properties.²² Transition metal dichalcogenides such as molybdenum disulfide (MoS₂) have been synthesized and utilized for a wide range of applications, such as sensing,²³ electrocatalysts,²⁴ supercapacitors²⁵ and energy storage systems.^{26–29} However, the widely known structure, namely, hexagonal MoS₂ (2H-MoS₂) with a trigonal prismatic coordination, is not the best candidate for electrode applications due to its semiconducting nature.²⁰ Several studies employed 2H-MoS₂ for electrochemical applications after improving its electronic conductivity *via* hybridization with carbon materials, *i.e.*, carbon nanotubes (CNTs),^{21,30,31} reduced graphene oxide,^{32,33} carbon nanofibers³⁴ and other forms of carbon.^{34–36}

The Mo edges are known to be the most catalytically active sites in MoS₂; thus, extensive research has been focused on increasing its edge density.³⁷ However, these metallic edges become rapidly deactivated by oxidation²⁷ or are covered with discharge products during the ORR in a LOB system. Ionic liquid (IL)-based electrolytes can suppress the oxidation through binding with the Mo edges to form isolated Mo sites.²⁷ MoS₂ nanoflakes (NFs) in an IL-based electrolyte survived for 50 cycles at an upper limit capacity of 500 mA h g⁻¹ and a current density of 0.1 mA cm⁻².²⁷ In another study, semiconducting MoS₂ nanosheets (NSs) decorated with Au NPs were used to prepare an oxygen electrode, which delivered a discharge capacity of 1000 mA h g⁻¹ for 50 cycles at 300 mA g⁻¹.²⁸ A cathode made of graphene aerogel decorated with MoS_x (1 < x < 2) NSs was also discharged for 30 cycles until the lower limit capacity of 500 mA h g⁻¹ at 0.1 mA cm⁻².²⁹

An octahedral coordination of metal atoms in metallic trigonal MoS₂ (1T-MoS₂) was achieved *via* the intercalation of alkali ions to form 1T-A_xMoS₂ (A = Li, Na, and K).^{38–44} The alkali-intercalated MoS₂ was exfoliated easier than the bulk MoS₂.^{45,46} Further solvation and liquid exfoliation resulted in stabilized 1T-MoS₂.^{38,47} Chemical exfoliation by alkali intercalation also modified the crystal structure due to electron transfer between the alkali compound, *e.g.* *n*-butyllithium, lithium borohydride and sodium naphthalenide, and the MoS₂ NSs.^{45,46,48} The theoretical analysis confirmed that the octahedral coordination favored the accommodation of these extra electrons in the d orbitals of the metal atoms, leading to the emergence of metallic properties.⁴⁹ Several studies showed higher catalytic activities for the stable metallic 1T-MoS₂ phase than the 2H-MoS₂ phase in hydrogen evolution reaction application.^{48,50–52} However, the use of the stable 1T-MoS₂ as an electrocatalyst in batteries is rare, which has only been reported for LIBs⁵³ and Na-ion batteries to date.⁵⁴ Thus, remains unexplained whether the structural changes to the conducting 1T-MoS₂ can influence the ORR and OER catalytic activities with respect to the electrochemical performance of LOBs.

Herein, 2D 1T-MoS₂ NSs were prepared *via* the intercalation of Na⁺ ions followed by exfoliation. Freestanding oxygen electrodes were prepared *via* the hybridization of the 2D NSs with 30 wt% functionalized CNTs, which were designated as 1T-MoS₂/CNT (method in Supplementary Note 1 in ESI†). The electrochemical performance of the 1T-MoS₂/CNT cathode in a

custom-built LOB cell^{55,56} was measured and compared with its 2H-MoS₂/CNT counterpart (Supplementary Note 3 in ESI†). The exfoliated 1T-MoS₂ electrocatalyst significantly enhanced the LOB performance due to its substantially improved electrical conductivity, enhanced access to the catalytically active sites by the electrolyte and elevated ionic and mass transport capability. Furthermore, a freestanding electrode design without binders can avoid the negative effects of binder in reducing the electrode conductivity and electrochemical performance.¹⁴ We used the density functional theory (DFT) (Supplementary Note 4 in ESI†) to predict the preferred paths for the initial oxygen reduction on different MoS₂ phases. The computation results combined with ORR and OER experiments using the rotational ring disc electrode (RRDE) (Supplementary Note 3 in ESI†) revealed the reasons behind the outstanding performance of the 1T-MoS₂ electrocatalysts in the LOB system. This work presents new insight into the application of metallic MoS₂ as a bifunctional oxygen electrocatalyst.

Results and discussion

Characterization of materials and structures

2D 1T-MoS₂ were formed *via in situ* liquid-redox intercalation followed by solvent exchange exfoliation. Solvent exchange was used to maintain the large lateral sizes of MoS₂ during the redox intercalation and exfoliation. *N*-Methyl-2-pyrrolidone (NMP) was found to be effective in reducing the thickness of pristine MoS₂ NFs, while the use of dimethylformamide (DMF) maintained the original lateral size of NSs.⁵⁷ The oxidative decomposition of NaBH₄ released H₂ and B₂H₆ gas according to eqn (1), generating stress to pre-expand the MoS₂ layered structure, thus aiding Na intercalation.^{41,48,58} The Na⁺ ions resulting from the decomposition of NaBH₄ (eqn (1)) and NaOH⁵⁹ (eqn (2)) in methanol intercalated into the pre-expanded MoS₂ interlayers to form 1T-Na_xMoS₂. It was shown by computations^{38,60} and experiments^{42–45} that upon Na intercalation, MoS₂ underwent a first-order phase transition to the octahedral coordination, where the Mo atoms formed the metallic 1T phase of MoS₂.⁴⁶



The strong reduction characteristics of borohydride ions, BH₄⁻, are necessary to transfer electrons to the S layer of 1T-Na_xMoS₂ to compensate for the created charge through Na intercalation and stabilize the 1T phase (Fig. 1a).^{41,45,58} The gases released during intercalation and the coulombic repulsion⁴¹ of the negatively charged 1T-Na_xMoS₂ resulted in high-yield liquid exfoliation. It is worth noting that the measurement of carrier concentration in the oxygen electrode indicated that 1T-MoS₂/CNT was negatively charged (Table S2†), while 2H-MoS₂/CNT was positively charged, similarly to CNTs.^{38,45}

The atomic force spectroscopy (AFM) analysis (Fig. 1b and c) revealed that the majority of 1T-MoS₂ NSs were 4–11 nm thick

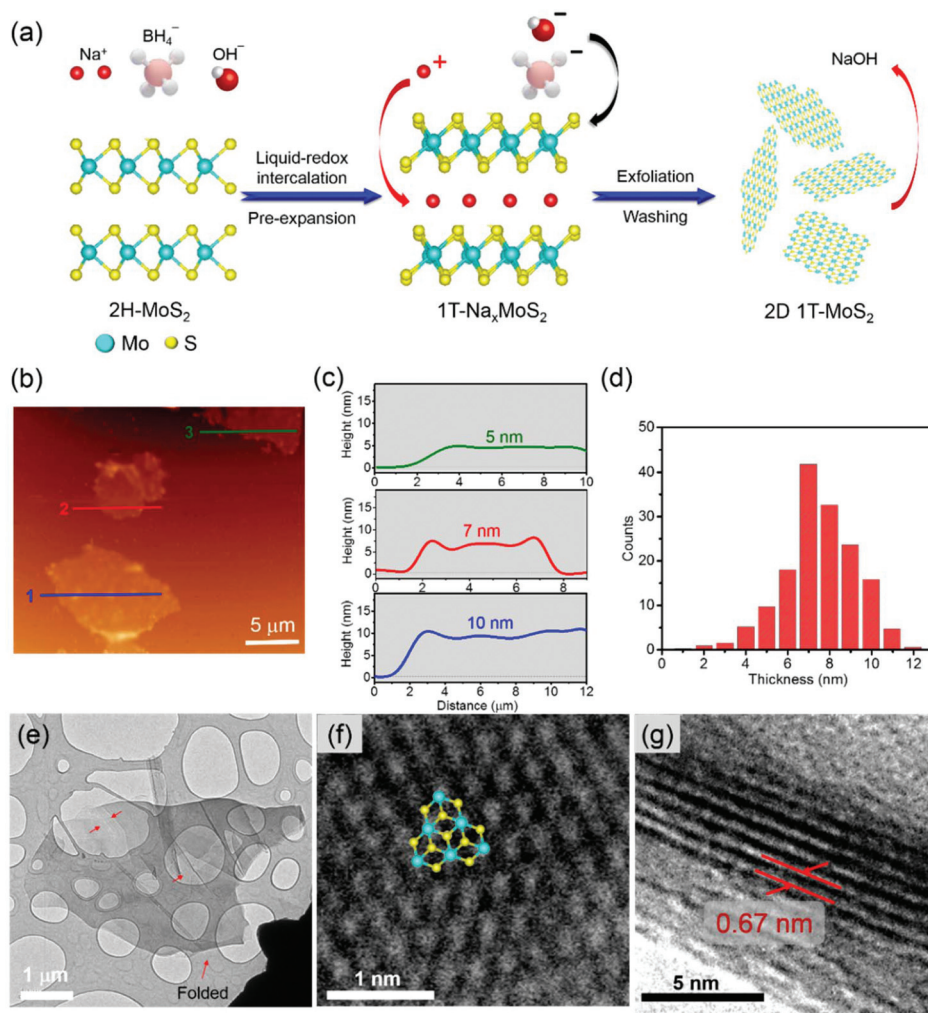


Fig. 1 (a) Illustration of the synthetic procedure. (b) AFM image of 1T-MoS₂. (c) Height profiles of the 1T-MoS₂ NSs from AFM. (d) Histogram of the thickness distribution of 1T-MoS₂. (e) TEM image of a 2D 1T-MoS₂ NS, in which the folded parts are indicated by arrows. (f) Magnified HRTEM view of the basal plane showing the individual Mo (blue dot) and S (yellow dot) atoms in 1T-MoS₂ with a triangular arrangement. (g) HRTEM image of the 1T-MoS₂ edge showing the MoS₂ layers.

in the exfoliated state, corresponding to 6–16 layers with one layer being 0.67 nm thick (Fig. 1g). The transmission electron microscopy (TEM) image presented few micron-sized 2D NSs with folded edges, as indicated by arrows (Fig. 1e). The magnified high-resolution TEM (HRTEM) image of the basal plane (Fig. 1f) revealed the triangular arrangement of individual Mo atoms (blue) in the 1T-MoS₂ phase, corresponding to the trigonal structure. The HRTEM image of the edge of 1T-MoS₂ (Fig. 1g) represented a similar thickness to the AFM results with a spacing of 0.67 nm between layers.

The exfoliated 1T-MoS₂ NSs presented a down-shifted (002) X-ray diffraction (XRD) peak located at $2\theta = 13.2^\circ$ compared to that of the bulk powder at $2\theta = 14.45^\circ$ (Fig. 2a). The (002) peak is attributed to the interplanar d -spacing between the (002) crystalline planes, and its down-shifting reflects the expansion of the planes. The oxidative decomposition of NaBH₄ and NaOH during sonication generated Na⁺ ions. These Na⁺ ions were intercalated into the gaps between the MoS₂ layers

bonded by weak van der Waals interactions, resulting in the expansion of the d -spacing. Considering the d -spacing of 0.612 nm in the bulk powder extracted from the XRD spectrum, the spacing of 0.67 nm was calculated for 1T-MoS₂ using Bragg's law ($n\lambda = 2d \sin \theta$), which is consistent with the HRTEM observation (Fig. 1g). The (002) peak was also broadened, representing the random arrangement of the NSs. Different phases were also identified using Raman spectroscopy (RS) and X-ray photoelectron spectroscopy (XPS) (Fig. 2b–d). The intercalation-induced phase transformation was confirmed by RS, where the J_1 to J_3 photon modes were activated at 150–300 cm⁻¹ for 1T-MoS₂ while they were absent for 2H-MoS₂ (Fig. 2b).^{40,46} The up-shifting of the E¹_{2g} peak, down-shifting of the A_{1g} peak and reduction in the intensity ratio, E¹_{2g}/A_{1g}, (Fig. 2b inset) observed for the 1T-MoS₂ phase indicate a reduction in the number of monolayers.⁶¹ The deconvoluted Mo 3d and S 2p XPS spectra also signify the conversion from the bulk MoS₂ powder to metallic 1T phase by Na

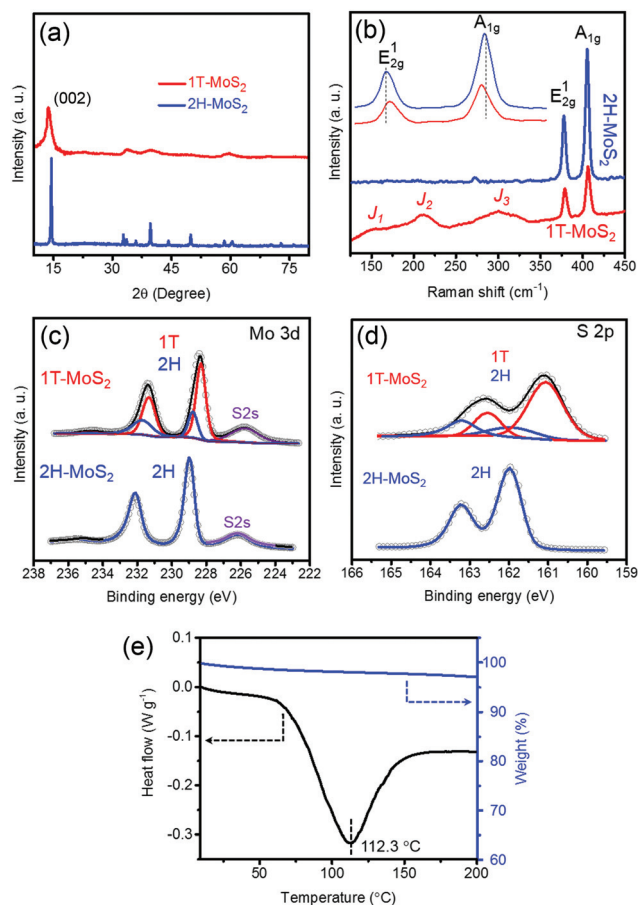


Fig. 2 (a) XRD spectra of exfoliated 1T-MoS₂ and bulk 2H-MoS₂. (b) Comparison of the RS for 1T- and 2H-MoS₂ (inset in b: E_{2g}¹ and A_{1g} peak shifts). XPS spectra with deconvoluted peaks of (c) Mo 3d and (d) S 2p. (e) TG-DSC curves of 1T-MoS₂.

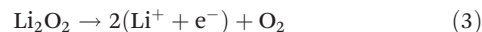
intercalation (Fig. 2c and d). The binding energies of the 1T phase peaks are located at ~228.2 and ~231.3 eV for Mo 3d and ~161.2 and ~162.5 eV for S 2p, which are ~0.8 eV lower than that of their 2H counterparts (Fig. 2c and d, respectively).²⁰ The thermostability of 1T-MoS₂ was studied using thermal gravimetry (TG) and differential scanning calorimetry (DSC) in an O₂ atmosphere at 20–200 °C (Fig. 2d). An exothermic peak centred at 112.3 °C was observed. However, a very slow weight reduction was observed with an increase in temperature, indicating a phase transformation from the 1T phase to the 2H phase at elevated temperature.

Judging from the oxygen electrode design, restacking of the exfoliated 1T-MoS₂ NSs (Fig. S2a†) during infiltration is detrimental to the electrode performance due to the lack of porosity required for O₂ flow and the storage of discharge products. If this happens, the cathode surface would be covered by Li₂O₂ reaction products and become insulated, causing a degradation in performance. Therefore, CNTs were added in this study to construct a 2D–1D hybrid structure, in which the 2D 1T-MoS₂ NSs were interleaved with 1D CNTs to prevent restacking (Fig. S2b†). The TEM image of 1T-MoS₂/CNT (Fig. S2c†)

showed that the CNTs were dispersed and attached on 1T-MoS₂ or wrapped between the 2D NSs. A uniform distribution of MoS₂ in the 1T-MoS₂/CNT electrode was seen from the elemental maps obtained from energy dispersive X-ray spectroscopy (Fig. S2d†).

Lithium–oxygen battery performance

Fig. 3a and b show the discharge/charge profiles of the different cathodes tested at a maximum capacity of 500 mA h g⁻¹ and 200 mA g⁻¹. At half of the upper-limit capacity, 250 mA h g⁻¹, the 1T-MoS₂ catalyst decreased both the discharge and charge overpotentials to 200 and 300 mV, respectively, compared to 2H-MoS₂ (Fig. 3a). The 2H-MoS₂/CNT cathode was not able to complete the targeted capacity before reaching the voltage limit for discharge (2 V) and charge (4.5 V), where its maximum capacity was about 400 mA h g⁻¹ in the first cycle (Fig. 3a). The charge plateau in the potential window of 0.4–1.2 V is attributed to the O₂ evolution from the bulk Li₂O₂, according to eqn (3). The kinetics of this reaction is sensitive to the catalytic activities of the catalyst in the oxygen electrode.⁶²



The corresponding charge plateau of the 1T-MoS₂/CNT cathode decreased from the 1st (4.05 V) through the 85th cycle (3.70 V) (Fig. 3b and e), reflecting the lower potential required for O₂ evolution in the bulk Li₂O₂ with increasing cycles. The *ex situ* XPS spectra indicated that 1T-MoS₂/CNT successfully decomposed the deposited Li₂O₂ layer (Fig. S3a†) with its peak at 54.8 eV completely disappearing after the 70th charge (Fig. S3c†). The comparison of the *ex situ* XRD spectra after the 20th discharge (Fig. S4a†) and the 70th recharge (Fig. S4b†) confirmed the reversible formation and decomposition of Li₂O₂ in the 1T-MoS₂/CNT electrode. Moreover, the HRTEM images taken from the edge of the 1T-MoS₂ layers illustrated the formation of Li₂O₂ after discharge and its decomposition after charge (Fig. S5†). This observation is partly responsible for the outstanding cyclic stability of the 1T-MoS₂/CNT cathode arising from its electrochemical activation. The required potential for O₂ evolution in its 2H-MoS₂/CNT counterpart rapidly increased during the first 10 cycles (Fig. 3c and f), which corroborates the inability of 2H-MoS₂ to catalyze the sluggish OER. When the required potential for O₂ evolution increased beyond 4.3 V (Fig. 3c), the decomposition of the electrolyte solvent resulted in the formation of RCOOLi. The *ex situ* XPS spectra showed a peak at ~56 eV, corresponding to the RCOOLi phase after the 5th discharge and the 10th charge (Fig. S3b and d†). The XPS results also indicated incomplete Li₂O₂ decomposition after the 10th charge in the 2H-MoS₂/CNT cathode, consistent with its weak catalytic ability (Fig. S3d†). However, for 1T-MoS₂/CNT, the same peak for RCOOLi was not detected after the 20th discharge, while its appearance after the 70th charge was related to the elevated charge potential after long cycles. For both electrodes, Li₂CO₃ (~55.4 eV) was formed due to the reaction between Li₂O₂ and CO₂, where CO₂ arose from the oxidation of the CNT

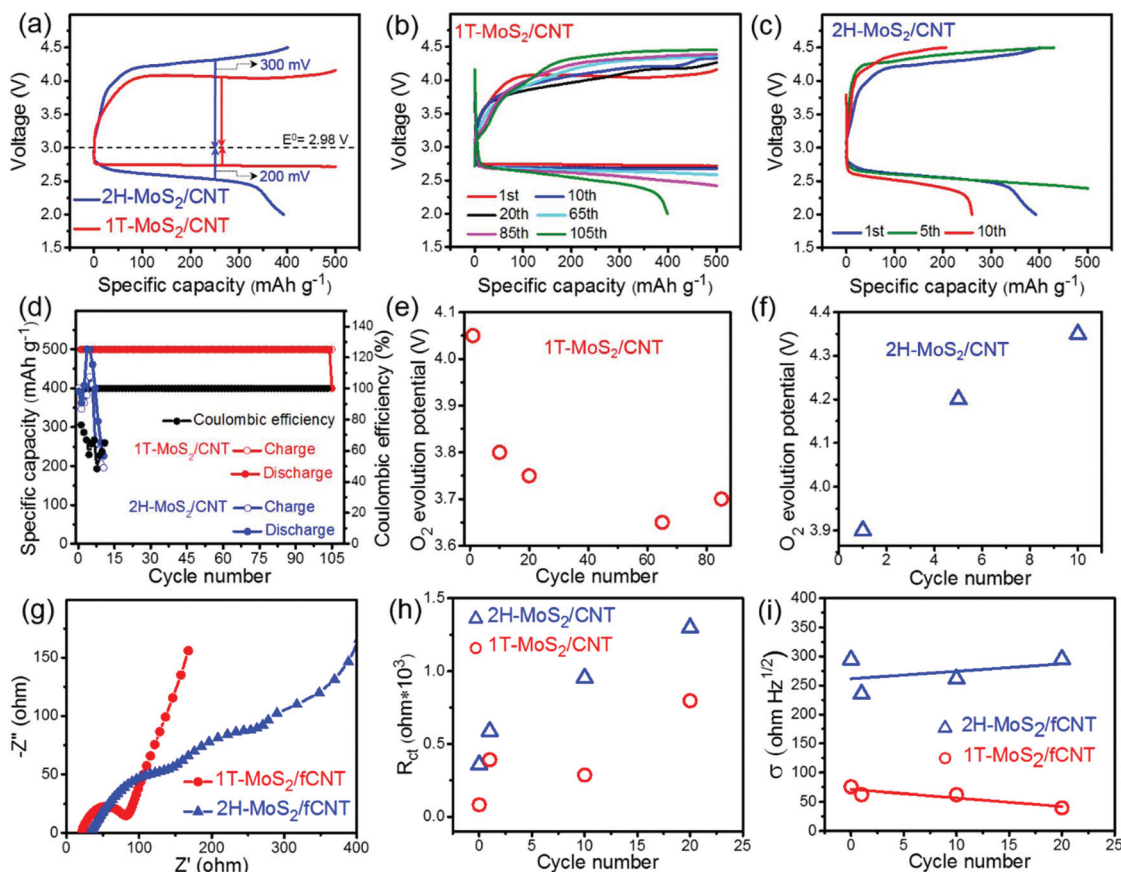


Fig. 3 Comparison of the discharge/charge curves of LOBs with the 1T-MoS₂/CNT and 2H-MoS₂/CNT cathodes at a current density of 200 mA g⁻¹ with an upper-limit capacity of 500 mA h g⁻¹ in the (a) first cycle and (b and c) following cycles. (d) Cyclic performance at the upper limit capacity and coulombic efficiencies of the 1T-MoS₂/CNT and 2H-MoS₂/CNT cathodes. O₂ evolution potential versus cycle number of (e) 1T-MoS₂/CNT and (f) 2H-MoS₂/CNT corresponding to the charge plateau in (b) and (c), respectively. Comparison of (g) EIS curves before cycles and (h) charge transfer resistance (R_{ct}) and (i) Warburg factor (σ) after the first, 10th and 20th cycles for the 1T-MoS₂/CNT and 2H-MoS₂/CNT cathodes.

surface.^{63,64} The 1T-MoS₂/CNT cathode survived for over 100 cycles (Fig. 3b and d) at the upper-limit capacity of 500 mA h g⁻¹ and at a current density of 200 mA g⁻¹ with a remarkable coulombic efficiency of 100% (Fig. 3d). In contrast, its 2H-MoS₂/CNT counterpart exhibited unstable behavior from the first cycle (Fig. 3c) with very poor coulombic efficiencies (Fig. 3d).

The electrochemical impedance spectroscopy (EIS) spectra of the fresh 1T-MoS₂/CNT and 2H-MoS₂/CNT electrodes are compared in Fig. 3g; the impedance parameters presented in Table S1† were analyzed using the Zview software with their corresponding equivalent circuits (insets in Fig. S6b and c†). 1T-MoS₂/CNT presented a considerably lower charge transfer resistance, R_{ct} , than 2H-MoS₂/CNT (Table S1†) due to its much higher electrical conductivity of 54.6 vs. 10.7 S cm⁻¹ (Table S2†). The electronic density of states (DOS) of 1T- and 2H-MoS₂ (Fig. 4a and b) were studied *via* DFT calculations and the comparison clearly indicated the metallic behavior of the former due to the lack of a bandgap and the semiconducting behavior of the latter with a bandgap of 0.74 eV. The underestimation of the calculated bandgaps compared to the experimental value, 1.2 eV,²⁰ is a drawback of generalized gradient

approximation calculations, as noted previously.⁶⁵ The much lower diffusion resistance, Z_w , (Table S1†) for 1T-MoS₂/CNT than 2H-MoS₂/CNT represents its dominant mass transport. This in turn allowed faster Li⁺ and O₂ transport across the interface between the cathode and Li₂O₂, which kinetically drove the evolution reaction (OER, eqn (3)) for the facile decomposition of Li₂O₂. The above discussion is partly proven by the almost two orders of magnitude higher lithium diffusion coefficient, D_{Li} , of 1T-MoS₂/CNT than 2H-MoS₂/CNT, *i.e.* 9.9×10^{-10} vs. 1.8×10^{-11} cm² s⁻¹ (Table S2†). These values were determined from the cyclic voltammetry curves in the third and following cycles at different scan rates (Fig. S6d and e†) (Supplementary Note 5 in ESI†).

The *ex situ* EIS analysis (Fig. S6b and c†) after cycles gave a clearer picture of the enhanced catalytic activities of the 1T-MoS₂ electrode. Fig. 3h and i compare the R_{ct} and Warburg factor (σ , Supplementary Note 6 in ESI†) taken from the EIS curves at different stages of cycles (Fig. S6b and c†). The lower R_{ct} values for 1T-MoS₂/CNT than 2H-MoS₂/CNT in the 20th cycle (Fig. 3h) revealed its faster transfer of charge species (Li⁺ and e⁻) due to its higher reaction kinetics for both the ORR

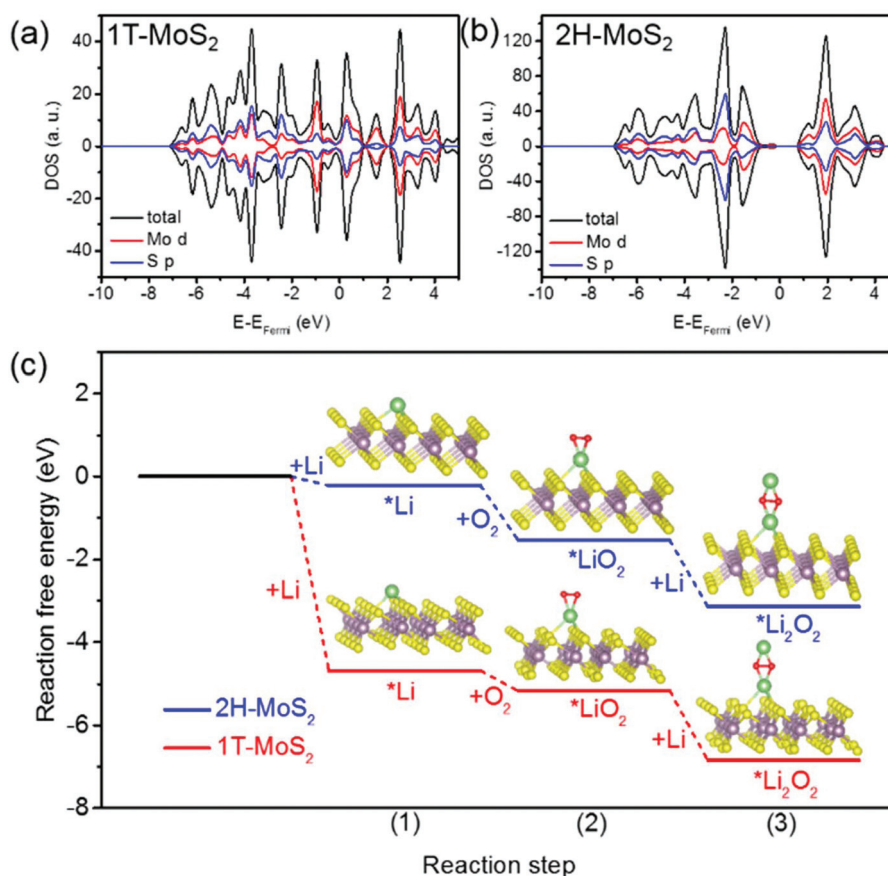


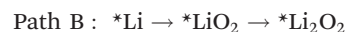
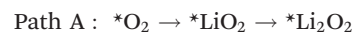
Fig. 4 Total and partial electronic DOSs calculated for (a) 1T-MoS₂ and (b) 2H-MoS₂. (c) Reaction free energies for the formation of Li₂O₂ on the 1T-MoS₂ and 2H-MoS₂ surfaces according to Path B: *Li → *LiO₂ → *Li₂O₂. The asterisks refer to the surface-adsorbed species.

and OER. Furthermore, throughout the first 20 cycles, the σ of 1T-MoS₂/CNT was generally lower than that of 2H-MoS₂/CNT (Fig. 3i). The inverse relationship between σ^2 and D_{Li} (eqn (S9)[†])⁶⁶ indicates that the former electrode has a higher lithium diffusivity with a decreasing growth rate in the first 20 cycles (Fig. 3i), resulting in its enhanced cyclic and coulombic efficiencies. In summary, the LOB performance study demonstrated the enhanced capability of the exfoliated metallic 1T-MoS₂ catalyst to reduce O₂ during the ORR and to decompose Li₂O₂ during the OER.

Mechanistic understanding with DFT computations

A mechanistic analysis was performed using DFT calculations⁶⁷ to investigate the initial ORR mechanism. The result presented below further supports the outstanding performance of the 1T-MoS₂ catalyst during the ORR. In the LOB system, discharge initiates when the Li atom is oxidized to release electrons to the external circuit and produce Li⁺ ions to meet the reduced oxygen molecules (O₂⁻) at the cathode surface.⁴ Therefore, it can be speculated that the main discharge products in the aprotic LOB system, Li₂O₂, arose from two different possible reaction paths, depending on the adsorption energies of the initially adsorbed species and the catalytic activity of the cathode surface.^{68,69} The two possible

reaction paths are given below, where the asterisks refer to the surface-adsorbed species:



Whether one path is more dominant than the other is determined by the rate of adsorption between the O₂ and Li species.⁷⁰ Therefore, the adsorption energies were calculated on both 2H-MoS₂ and 1T-MoS₂, and both the Mo edges and basal planes were also considered for the calculation of the O₂ adsorption energies. The results given in Table S3[†] show that the adsorption energies on the edges of the 2H- and 1T-phases of -9.247 and -8.622 eV were very competitive compared to the corresponding values on the basal planes of -0.095 and -2.885 eV, respectively. The strong adsorption energies of O₂ molecules on the exposed Mo edges of both 2H-MoS₂ and 1T-MoS₂ resulted in the dissociation of the O₂ molecules to form two bound O atoms on the Mo edges (see the configuration in Table S3[†]). The continued dissociation of O₂ molecules led to fully oxidized Mo edges, which did not favor oxygen reduction.²⁷ In the ORR process according to Path A, the O₂ molecules are required to bind on the surface of the cathode followed by reduction to form an adsorbed species,

O_2^{-*} ($e^- + O_2^* \rightarrow O_2^{-*}$). However, due to the strong adsorption energies of the O_2 molecules and their dissociation on the Mo edges of 2H-MoS₂ and 1T-MoS₂, the O_2^{-*} species could not be formed to allow the ORR to occur according to Path A. It is reported that only in some places where the Mo edges are partially oxidized, O_2 can bind with an exposed Mo atom in isolation to reduce to O_2^{-*} through charge transfer.²⁷ However, the strong adsorption energies of O_2 on the edges most likely drive the reaction toward the full oxidation of the Mo edges and contaminate the catalyst. The poor LOB performance of the 2H-MoS₂/CNT cathode (Fig. 3c and d) reflects its weak catalytic activities. The passivation of the metallic Mo edges by oxidation in 2H-MoS₂ and no ORR catalytic activity of the basal planes were mainly responsible for the degradation of the LOB performance of 2H-MoS₂/CNT.

To continue revealing the initial ORR path, the adsorption energies of O_2 and Li on the basal planes were investigated. O_2 can be adsorbed on the Mo surface at a distance of ~ 4.5 Å (see the configuration in Table S3†), which prevents the transfer of electrons between the catalyst surface and O_2 to reduce it to O_2^{-*} . Therefore, Path A favors the adsorption of neither the 2H- nor 1T-phase on the edges and basal planes. To investigate the reaction energies of Path B, the Li adsorption energies on the basal planes were calculated for two different possible sites, namely, the top of an Mo atom (T) and the hollow position (H) (see the configuration in Table S4†). The adsorption energies (Table S4†) suggest that Li favored the Mo atom (T), where the stable position of Li deviated from the right above

Mo in 1T-MoS₂, as shown in the corresponding configuration. Similar findings on the most stable sites, the deviation of the Mo position and the adsorption energies were reported previously.^{71,72} The much stronger adsorption energy of Li on 1T-MoS₂ (-4.68 eV) than on 2H-MoS₂ (-0.22 eV) evidenced the higher affinity of the former surface to exhibit ORR activity through Path B. The adsorption energies of Li_xO_y compounds created by Path B on the two MoS₂ surfaces were calculated, as shown in Table S5.† When O_2 molecules were added, the stronger adsorption energy of Li_2O_2 on the 1T-MoS₂ surface of -6.842 eV than on the 2H-MoS₂ surface of -3.14 eV, led to its enhanced discharge capacity. The reaction free energies of the different steps according to Path B during the ORR from the 2H- and 1T-MoS₂ surfaces are shown in Fig. 4c. The higher energies released on the 1T-MoS₂ surface than on its 2H-MoS₂ counterpart are strongly correlated with its outstanding performance in LOBs.

Electrocatalytic activity toward the ORR and OER

The above DFT calculations verified that the better LOB performance of the 1T-MoS₂ catalyst is attributed to its catalytically active basal planes. However, it is necessary to confirm experimentally whether its outperformance is related to the intrinsic catalytic activity of 1T-MoS₂ due to its large active sites and/or the increased electronic conductivity of the metallic NSs with faster charge transport. Thus, we further explored the electrocatalytic activities toward the ORR (Fig. 5a) and OER (Fig. 5b) using an RRDE in O_2 -saturated 0.1 M KOH. The linear

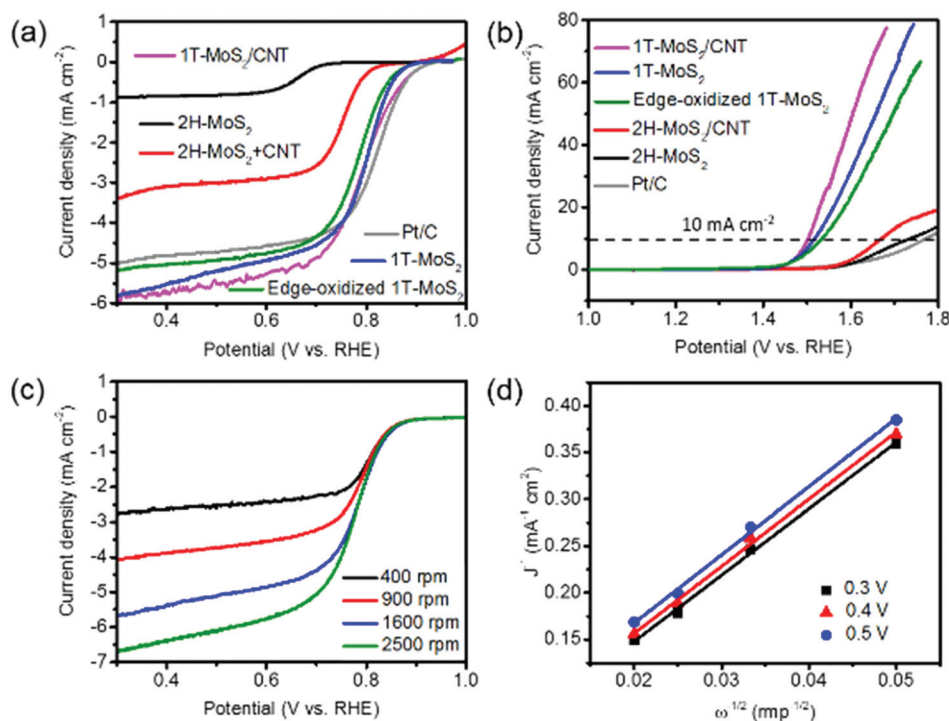


Fig. 5 Electrocatalytic activities of 1T-MoS₂, 1T-Na₂MoS₂, 1T-MoS₂/CNT, 2H-MoS₂, 2H-MoS₂/CNT and Pt/C in O_2 -saturated 0.1 M KOH: LSV curves for the (a) ORR and (b) OER at a rotating speed of 1600 rpm and 5 mV s^{-1} . (c) LSV curves for the ORR of 1T-MoS₂ at different rotating speeds. (d) K-L plots of 1T-MoS₂ based on the obtained LSV curves.

scanning voltammetry (LSV) curve of 1T-MoS₂ obtained during the ORR at 1600 rpm (Fig. 5a) presents a high onset-potential ($E_o \approx 0.9$ V). However, the onset-potential of 2H-MoS₂ substantially decreased ($E_o \approx 0.73$ V) due to the low concentration of active edges stemming from its large lateral dimensions and poor electronic conductivity. 1T-MoS₂ exhibited both a much higher half-wave potential ($E_{1/2}$) and diffusion-limited current density (j_L) ($E_{1/2} \approx 0.81$ V and $j_L \approx -5.8$ mA cm⁻²) than that of 2H-MoS₂ ($E_{1/2} \approx 0.66$ V and $j_L \approx -0.8$ mA cm⁻²). 1T-MoS₂ showed an almost equivalent $E_{1/2}$ and enhanced j_L compared to that of Pt/C ($E_{1/2} \approx 0.8$ V and $j_L \approx -5$ mA cm⁻²) (Fig. 5a). After the incorporation of 30 wt% CNTs, the onset potential of the 1T-MoS₂/CNT catalyst improved to the highest value of 0.94, which is almost the same as that measured for commercial Pt/C, $E_o \approx 0.95$ V.⁷³ The 1T-MoS₂/CNT catalyst presented similar values for $E_{1/2}$ and j_L to 1T-MoS₂. This finding reflects the high electrical conductivity of 1T-MoS₂, which may not change much even after the incorporation of CNTs, and the high catalytic activity of the basal planes in 1T-MoS₂ remained mostly unaffected by the physical mixture of CNTs.

The OER activity was studied in a higher positive region than the ORR to evaluate the bifunctional catalytic activity. As shown in Fig. 5b, the 1T-MoS₂ displayed an OER potential of ~ 1.52 V at 10 mA cm⁻², which is much lower than that of both 2H-MoS₂ (~ 1.73 V) and Pt/C (~ 1.78 V), indicating the exfoliated 1T-MoS₂ is a highly promising bifunctional ORR/OER catalyst compared to 2H-MoS₂. The addition of CNT to 1T-MoS₂ marginally enhanced its potential to ~ 1.5 V, illustrating the ameliorated OER activity of the 1T-MoS₂/CNT catalyst. A comparison of the ORR and OER activities of both 1T-MoS₂ and 2H-MoS₂ with that of recently studied MoS₂ electrocatalysts is shown in Table 1.^{73–77} Indeed, the 1T-MoS₂ catalyst presents a comparable performance for both the ORR and OER.

The influence of Mo edge passivation on the oxygen electrochemistry of the edge-oxidized 1T-MoS₂ was studied using the sodium-intercalated 1T NSs, which were kept in an aqueous solution for a few days at room temperature.⁴⁸ The oxidation of Mo edges was confirmed from the XPS spectrum, where two new peaks of MoO₃ appeared at 232.5 and 234 eV corresponding to Mo⁶⁺ 3d_{5/2} and Mo⁶⁺ 3d_{3/2}, respectively (Fig. S7†). It appears that the edge oxidation only slightly disrupted the metallic phase atomic arrangement according to the comparison of the 1T/2H ratios measured before (2.05) and after ox-

idation (1.83).⁴⁸ The 1T/2H ratios were measured by calculating the total area under the 1T and 2H deconvoluted peaks from the corresponding XPS spectra (Fig. 2c and S7†). The ORR measurement on the edge-oxidized 1T-MoS₂ showed only a marginal decrease in onset-potential (~ 0.89 V) compared to that of the pristine 1T-MoS₂. Furthermore, the slight differences between that measured after ($j_L \approx -5.2$ mA cm⁻² and $E_{1/2} \approx 0.79$ V) and before ($j_L \approx -5.8$ mA cm⁻² and $E_{1/2} \approx 0.81$ V) edge oxidation suggest only a small negative impact of edge passivation on the catalytic activities of 1T-MoS₂. Therefore, it can be concluded that the Mo edges in 1T-MoS₂ were not the only ORR catalytic active sites; rather, the basal planes mainly contributed to its ORR activities. The very small difference in OER potential found between the edge-oxidized 1T-MoS₂ (0.04 V) and neat 1T-MoS₂ (Fig. 5b) at a current density of 10 mA cm⁻² signified the very similar OER activities of both catalysts.

The ORR and OER activities of 2H-MoS₂/CNT was studied by measuring the influence of enhanced electrical conductivity on oxygen electrochemistry. An ORR onset-potential of ~ 0.8 V was achieved for 2H-MoS₂/CNT, which was similar to that of the neat 1T-MoS₂ and 1T-MoS₂/CNT (Fig. 5a), but not 2H-MoS₂. However, the increase in electrical conductivity of 2H-MoS₂ after the addition of CNTs slightly decreased its OER potential to 1.67 V at 10 mA cm⁻². In summary, the superior catalytic activity of the exfoliated 1T-MoS₂ is attributed to the synergistic effect of its metallic properties and catalytically active basal planes. The metallic properties facilitate efficient charge transfer, while the basal planes maximize the exposure of reaction sites, giving rise to promising bifunctional ORR/OER catalytic activities.

The larger catalytically active area in 1T-MoS₂/CNT than 2H-MoS₂/CNT was further investigated by estimating the electrocatalytically active surface areas (ECSAs) using the cyclic voltammetry (CV) curves (Fig. 6a and b). The current response in the potential window of 0.91–1.11 V vs. RHE at different scan rates (40–180 mV s⁻¹) arose from the charging of the double-layer.⁷⁸ The double-layer capacitance (C_{dl}), which is directly proportional to the ECSA,^{78,79} was estimated by plotting the current difference ($\Delta J = J_a - J_c$) at a given potential (1 V vs. RHE) against the CV scan rate, as shown in Fig. 6c. The C_{dl} was almost nine times larger for 1T-MoS₂/CNT (27 mF cm⁻²) than 2H-MoS₂/CNT (3.1 mF cm⁻²), which agrees well with its much larger ECSA (84.7 cm² vs. 9.7 cm²). Supplementary Note

Table 1 Comparison of the ORR and OER performances of various MoS₂-based catalysts

Sample	ORR		OER		Ref.
	Onset potential (V vs. RHE)	Half-wave potential ($E_{1/2}$, V vs. RHE)	Diffusion-limited current (j_L , mA cm ⁻²)	OER potential at 10 mA cm ⁻² (V vs. RHE)	
1T-MoS ₂	0.9	0.81	-5.8	~ 1.52	This work
2H-MoS ₂	0.73	0.66 V	-0.8	~ 1.75	
MoS ₂ with oxygen heteroatoms	0.94 (2400 rpm)	0.8	-3.4	—	74
Mo-N/C@MoS ₂	0.9 (1600 rpm)	0.81	-5.3	~ 1.62	73
CoMoS ₃ nanotubes	—	—	—	1.47	75
MoS ₂ /Ni ₃ S ₂	—	—	—	1.56	76
MoS ₂ -rGO	0.7	0.8	2.7	—	77

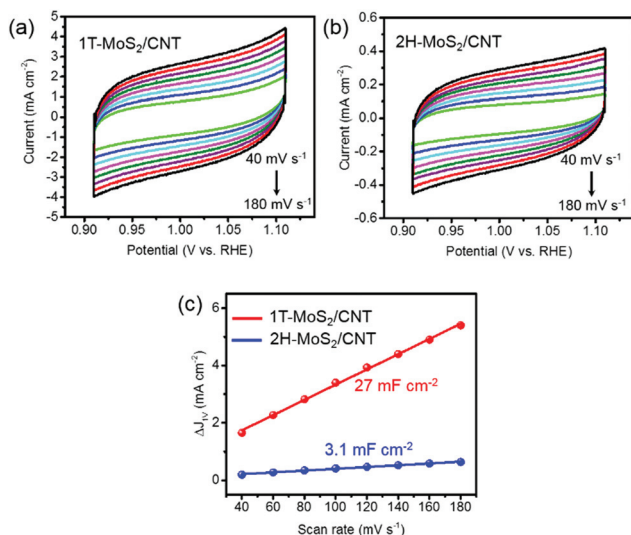


Fig. 6 CV curves of (a) 1T-MoS₂/CNT and (b) 2H-MoS₂/CNT in the potential range of 0.91–1.11 V vs. RHE at various scan rates (40–180 mV s⁻¹) and (c) linear fitting of the corresponding current densities measured at 1.0 V vs. RHE and different scan rates to estimate the C_{dl} from the slope.

3 in ESI† presents the ECSA calculations. The increase in ECSA demonstrates the proliferation of active sites, also signifying the contribution of 1T-MoS₂ to the improved catalytic performance.

The LSV curves obtained at different rotation speeds (Fig. 5c) were used to investigate the electron transfer kinetics during the ORR for 1T-MoS₂. When the rotation speed was increased from 400 to 2500 rpm, the current density increased due to the enhanced convective mass transfer of oxygen molecules from the electrolyte to the electrode surface. The linearity and parallelism of the Koutecky–Levich (K–L) plots (Fig. 5d) at various potentials indicate a first-order relationship between the reaction rate and the dissolved oxygen concentration.⁸⁰ The electron transfer number (n) calculated (Supplementary Note 3 in ESI†) from the slopes of the K–L plots ranged from 3.79–3.83, representing a four-electron transfer process for the 1T-MoS₂ phase.

Conclusions

2D metallic 1T-MoS₂ was prepared *via* the *in situ* liquid-redox intercalation of sodium ions and solvent exchange exfoliation, which was applied as a catalyst for oxygen electrodes in Li–O₂ batteries (LOBs) for the first time. The hybrid cathode consisting of 1T-MoS₂ and 30 wt% functionalized CNTs (1T-MoS₂/CNT) substantially outperformed its 2H-MoS₂/CNT counterpart. The freestanding and binder-free 1T-MoS₂/CNT cathode delivered a high capacity of 500 mA h g⁻¹ for more than 100 cycles at a current density of 200 mA g⁻¹. The results from *ex situ* EIS after LOB cycles confirmed the excellent charge and mass transfer across the 1T-MoS₂/CNT cathode, which facili-

tated the formation and decomposition of Li₂O₂ during the ORR and OER. The high electrical conductivity and large density of catalytically active sites in the 1T-MoS₂/CNT electrode were mainly responsible for its outstanding catalytic performance. The DFT calculations predicted the initiation of discharge on the basal planes of 1T-MoS₂ with the strong surface-adsorption of Li following the (*Li → *LiO₂ → *Li₂O₂) ORR path. In addition, the RRDE test revealed that the synergistic effects of both high electrical conductivity and catalytic activation of basal planes on the ameliorated ORR and OER activities make the 1T-MoS₂ electrode a much better electrocatalyst for LOBs than its 2H-MoS₂ counterpart.

Author contribution

All experiments were carried out by ZS and the DFT calculations were conducted by JL and FC. The manuscript was written by ZS and JKK. All authors have given approval to the final version of the manuscript.

Conflicts of interest

There are no conflicts to declare.

Acknowledgements

This project was financially supported by the Innovation and Technology Commission (ITS/001/17) and the Research Grants Council (GRF Projects: 16212814, 16208718) of Hong Kong SAR. The authors also appreciate the technical assistance from the Materials Characterization and Preparation Facilities (MCPF) and the Advanced Engineering Materials Facilities (AEMF) of HKUST.

References

- 1 Y. Zhang, K. Rui, Z. Ma, W. Sun, Q. Wang, P. Wu, Q. Zhang, D. Li, M. Du, W. Zhang, H. Lin and J. Zhu, *Chem. Mater.*, 2018, **30**, 4762–4769.
- 2 K. Rui, G. Zhao, Y. Chen, Y. Lin, Q. Zhou, J. Chen, J. Zhu, W. Sun, W. Huang and S. X. Dou, *Adv. Funct. Mater.*, 2018, **28**, 1801554.
- 3 D. Li, D. Wang, K. Rui, Z. Ma, L. Xie, J. Liu, Y. Zhang, R. Chen, Y. Yan, H. Lin, X. Xie, J. Zhu and W. Huang, *J. Power Sources*, 2018, **384**, 27–33.
- 4 D. Aurbach, B. D. McCloskey, L. F. Nazar and P. G. Bruce, *Nat. Energy*, 2016, **1**, 16128.
- 5 X. Gao, Y. Chen, L. Johnson and P. G. Bruce, *Nat. Mater.*, 2016, **15**, 882–888.
- 6 H.-G. Jung, J. Hassoun, J.-B. Park, Y.-K. Sun and B. Scrosati, *Nat. Chem.*, 2012, **4**, 579–585.

- 7 Y. Lin, B. Moitoso, C. Martinez-Martinez, E. D. Walsh, S. D. Lacey, J.-W. Kim, L. Dai, L. Hu and J. W. Connell, *Nano Lett.*, 2017, **17**, 3252–3260.
- 8 Y.-C. Lu, Z. Xu, H. A. Gasteiger, S. Chen, K. Hamad-Schifferli and Y. Shao-Horn, *J. Am. Chem. Soc.*, 2010, **132**, 12170–12171.
- 9 J. Huang, Z. Jin, Z.-L. Xu, L. Qin, H. Huang, Z. Sadighi, S. Yao, J. Cui, B. Huang and J.-K. Kim, *Energy Storage Mater.*, 2017, **8**, 110–118.
- 10 J. Huang, B. Zhang, Z. Bai, R. Guo, Z.-L. Xu, Z. Sadighi, L. Qin, T.-Y. Zhang, G. Chen, B. Huang and J.-K. Kim, *Adv. Funct. Mater.*, 2016, **26**, 8290–8299.
- 11 H. Wang, Y. Yang, Y. Liang, G. Zheng, Y. Li, Y. Cui and H. Dai, *Energy Environ. Sci.*, 2012, **5**, 7931–7935.
- 12 P. Sennu, M. Christy, V. Aravindan, Y.-G. Lee, K. S. Nahm and Y.-S. Lee, *Chem. Mater.*, 2015, **27**, 5726–5735.
- 13 Z. Ma, X. Yuan, Z. Zhang, D. Mei, L. Li, Z.-F. Ma, L. Zhang, J. Yang and J. Zhang, *Sci. Rep.*, 2015, **5**, 18199.
- 14 S. Liu, M. Wang, X. Sun, N. Xu, J. Liu, Y. Wang, T. Qian and C. Yan, *Adv. Mater.*, 2018, **30**, 1704898.
- 15 J. Huang, B. Zhang, Y. Y. Xie, W. W. K. Lye, Z.-L. Xu, S. Abouali, M. A. Garakani, J.-Q. Huang, T.-Y. Zhang, B. Huang and J.-K. Kim, *Carbon*, 2016, **100**, 329–336.
- 16 J.-J. Xu, D. Xu, Z.-L. Wang, H.-G. Wang, L.-L. Zhang and X.-B. Zhang, *Angew. Chem., Int. Ed.*, 2013, **52**, 3887–3890.
- 17 W.-J. Kwak, K. C. Lau, C.-D. Shin, K. Amine, L. A. Curtiss and Y.-K. Sun, *ACS Nano*, 2015, **9**, 4129–4137.
- 18 E. Yoo and H. Zhou, *ACS Nano*, 2011, **5**, 3020–3026.
- 19 P. Zhang, R. Wang, M. He, J. Lang, S. Xu and X. Yan, *Adv. Funct. Mater.*, 2016, **26**, 1354–1364.
- 20 M. Acerce, D. Voiry and M. Chhowalla, *Nat. Nanotechnol.*, 2015, **10**, 313.
- 21 J.-Z. Wang, L. Lu, M. Lotya, J. N. Coleman, S.-L. Chou, H.-K. Liu, A. I. Minett and J. Chen, *Adv. Energy Mater.*, 2013, **3**, 798–805.
- 22 M. Chhowalla, H. S. Shin, G. Eda, L.-J. Li, K. P. Loh and H. Zhang, *Nat. Chem.*, 2013, **5**, 263.
- 23 P. A. Lieberzeit, A. Afzal, A. Rehman and F. L. Dickert, *Sens. Actuators, B*, 2007, **127**, 132–136.
- 24 J. Xie, H. Zhang, S. Li, R. Wang, X. Sun, M. Zhou, J. Zhou, X. W. D. Lou and Y. Xie, *Adv. Mater.*, 2013, **25**, 5807–5813.
- 25 L. Zhang, H. Bin Wu, Y. Yan, X. Wang and X. W. D. Lou, *Energy Environ. Sci.*, 2014, **7**, 3302–3306.
- 26 Z. Hu, L. Wang, K. Zhang, J. Wang, F. Cheng, Z. Tao and J. Chen, *Angew. Chem.*, 2014, **126**, 13008–13012.
- 27 M. Asadi, B. Kumar, C. Liu, P. Phillips, P. Yasaei, A. Behranginia, P. Zapol, R. F. Klie, L. A. Curtiss and A. Salehi-Khojin, *ACS Nano*, 2016, **10**, 2167–2175.
- 28 P. Zhang, X. Lu, Y. Huang, J. Deng, L. Zhang, F. Ding, Z. Su, G. Wei and O. G. Schmidt, *J. Mater. Chem. A*, 2015, **3**, 14562–14566.
- 29 L. Li, C. Chen, J. Su, P. Kuang, C. Zhang, Y. Yao, T. Huang and A. Yu, *J. Mater. Chem. A*, 2016, **4**, 10986–10991.
- 30 J. Li, Y. Hou, X. Gao, D. Guan, Y. Xie, J. Chen and C. Yuan, *Nano Energy*, 2015, **16**, 10–18.
- 31 X. Li, J. Zhang, R. Wang, H. Huang, C. Xie, Z. Li, J. Li and C. Niu, *Nano Lett.*, 2015, **15**, 5268–5272.
- 32 L. David, R. Bhandavat and G. Singh, *ACS Nano*, 2014, **8**, 1759–1770.
- 33 F. Xiong, Z. Cai, L. Qu, P. Zhang, Z. Yuan, O. K. Asare, W. Xu, C. Lin and L. Mai, *ACS Appl. Mater. Interfaces*, 2015, **7**, 12625–12630.
- 34 C. Zhu, X. Mu, P. A. van Aken, Y. Yu and J. Maier, *Angew. Chem., Int. Ed.*, 2014, **53**, 2152–2156.
- 35 X.-Y. Yu, H. Hu, Y. Wang, H. Chen and X. W. D. Lou, *Angew. Chem., Int. Ed.*, 2015, **54**, 7395–7398.
- 36 J. Wu, Z. Lu, K. Li, J. Cui, S. Yao, M. I. Haq, B. Li, Q.-H. Yang, F. Kang, F. Ciucci and J.-K. Kim, *J. Mater. Chem. A*, 2018, **6**, 5668–5677.
- 37 K. D. Rasamani, F. Alimohammadi and Y. Sun, *Mater. Today*, 2017, **20**, 83–91.
- 38 M. Mortazavi, C. Wang, J. Deng, V. B. Shenoy and N. V. Medhekar, *J. Power Sources*, 2014, **268**, 279–286.
- 39 X. Wang, X. Shen, Z. Wang, R. Yu and L. Chen, *ACS Nano*, 2014, **8**, 11394–11400.
- 40 Z. Chen, K. Leng, X. Zhao, S. Malkhandi, W. Tang, B. Tian, L. Dong, L. Zheng, M. Lin, B. S. Yeo and K. P. Loh, *Nat. Commun.*, 2017, **8**, 14548.
- 41 E. D. Grayfer, M. N. Kozlova and V. E. Fedorov, *Adv. Colloid Interface Sci.*, 2017, **245**, 40–61.
- 42 S. H. Song, B. H. Kim, D.-H. Choe, J. Kim, D. C. Kim, D. J. Lee, J. M. Kim, K. J. Chang and S. Jeon, *Adv. Mater.*, 2015, **27**, 3152–3158.
- 43 V. K. Srivastava, R. A. Quinlan, A. L. Agapov, J. R. Dunlap, K. M. Nelson, E. Duranty, A. P. Sokolov, G. S. Bhat and J. W. Mays, *Adv. Funct. Mater.*, 2014, **24**, 4969–4977.
- 44 S. M. Tan, Z. Sofer, J. Luxa and M. Pumera, *ACS Catal.*, 2016, **6**, 4594–4607.
- 45 J. Zheng, H. Zhang, S. Dong, Y. Liu, C. T. Nai, H. S. Shin, H. Y. Jeong, B. Liu and K. P. Loh, *Nat. Commun.*, 2014, **5**, 2995.
- 46 G. Eda, H. Yamaguchi, D. Voiry, T. Fujita, M. Chen and M. Chhowalla, *Nano Lett.*, 2011, **11**, 5111–5116.
- 47 A. N. Enyashin, L. Yadgarov, L. Houben, I. Popov, M. Weidenbach, R. Tenne, M. Bar-Sadan and G. Seifert, *J. Phys. Chem. C*, 2011, **115**, 24586–24591.
- 48 D. Voiry, M. Salehi, R. Silva, T. Fujita, M. Chen, T. Asefa, V. B. Shenoy, G. Eda and M. Chhowalla, *Nano Lett.*, 2013, **13**, 6222–6227.
- 49 G. Eda, T. Fujita, H. Yamaguchi, D. Voiry, M. Chen and M. Chhowalla, *ACS Nano*, 2012, **6**, 7311–7317.
- 50 Y. Yin, J. Han, Y. Zhang, X. Zhang, P. Xu, Q. Yuan, L. Samad, X. Wang, Y. Wang, Z. Zhang, P. Zhang, X. Cao, B. Song and S. Jin, *J. Am. Chem. Soc.*, 2016, **138**, 7965–7972.
- 51 H. Wang, Z. Lu, S. Xu, D. Kong, J. J. Cha, G. Zheng, P.-C. Hsu, K. Yan, D. Bradshaw, F. B. Prinz and Y. Cui, *Proc. Natl. Acad. Sci. U. S. A.*, 2013, **110**, 19701–19706.
- 52 M. A. Lukowski, A. S. Daniel, F. Meng, A. Forticaux, L. Li and S. Jin, *J. Am. Chem. Soc.*, 2013, **135**, 10274–10277.

- 53 T. Xiang, Q. Fang, H. Xie, C. Wu, C. Wang, Y. Zhou, D. Liu, S. Chen, A. Khalil, S. Tao, Q. Liu and L. Song, *Nanoscale*, 2017, **9**, 6975–6983.
- 54 X. Geng, Y. Jiao, Y. Han, A. Mukhopadhyay, L. Yang and H. Zhu, *Adv. Funct. Mater.*, 2017, **27**, 1702998.
- 55 Z. Sadighi, J. Liu, F. Ciucci and J.-K. Kim, *Nanoscale*, 2018, **10**, 15588–15599.
- 56 Z. Sadighi, J. Huang, L. Qin, S. Yao, J. Cui and J.-K. Kim, *J. Power Sources*, 2017, **365**, 134–147.
- 57 F. Ghasemi and S. Mohajerzadeh, *ACS Appl. Mater. Interfaces*, 2016, **8**, 31179–31191.
- 58 J. Zhu, H. Wang, J. Liu, L. Ouyang and M. Zhu, *Nanotechnology*, 2017, **28**, 115604.
- 59 G. Zhao, S. Han, A. Wang, Y. Wu, M. Zhao, Z. Wang and X. Hao, *Adv. Funct. Mater.*, 2015, **25**, 5292–5299.
- 60 H. He, P. Lu, L. Wu, C. Zhang, Y. Song, P. Guan and S. Wang, *Nanoscale Res. Lett.*, 2016, **11**, 330.
- 61 C. Lee, H. Yan, L. E. Brus, T. F. Heinz, J. Hone and S. Ryu, *ACS Nano*, 2010, **4**, 2695–2700.
- 62 Y.-C. Lu and Y. Shao-Horn, *J. Phys. Chem. Lett.*, 2012, **4**, 93–99.
- 63 M. M. O. Thotiyl, S. A. Freunberger, Z. Peng, Y. Chen, Z. Liu and P. G. Bruce, *Nat. Mater.*, 2013, **12**, 1050.
- 64 M. M. Ottakam Thotiyl, S. A. Freunberger, Z. Peng and P. G. Bruce, *J. Am. Chem. Soc.*, 2012, **135**, 494–500.
- 65 L. Wei, C. Jun-fang, H. Qinyu and W. Teng, *Physica B: Condens. Matter*, 2010, **405**, 2498–2502.
- 66 J. Cui, S. Yao, J.-Q. Huang, L. Qin, W. G. Chong, Z. Sadighi, J. Huang, Z. Wang and J.-K. Kim, *Energy Storage Mater.*, 2017, **9**, 85–95.
- 67 S. Yao, J. Cui, Z. Lu, Z.-L. Xu, L. Qin, J. Huang, Z. Sadighi, F. Ciucci and J.-K. Kim, *Adv. Energy Mater.*, 2017, **7**, 1602149.
- 68 X. Li, Z. Li, X. Yang, L. Jia, Y. Q. Fu, B. Chi, J. Pu and J. Li, *J. Mater. Chem. A*, 2017, **5**, 3320–3329.
- 69 G. Girishkumar, B. McCloskey, A. C. Luntz, S. Swanson and W. Wilcke, *J. Phys. Chem. Lett.*, 2010, **1**, 2193–2203.
- 70 B. G. Kim, H.-J. Kim, S. Back, K. W. Nam, Y. Jung, Y.-K. Han and J. W. Choi, *Sci. Rep.*, 2014, **4**, 4225.
- 71 B. Xu, L. Wang, H. J. Chen, J. Zhao, G. Liu and M. S. Wu, *Comput. Mater. Sci.*, 2014, **93**, 86–90.
- 72 X. Sun, Z. Wang, Z. Li and Y. Q. Fu, *Sci. Rep.*, 2016, **6**, 26666.
- 73 I. S. Amiin, Z. Pu, X. Liu, K. A. Owusu, H. G. R. Monestel, F. O. Boakye, H. Zhang and S. Mu, *Adv. Funct. Mater.*, 2017, **27**, 1702300.
- 74 H. Huang, X. Feng, C. Du, S. Wu and W. Song, *J. Mater. Chem. A*, 2015, **3**, 16050–16056.
- 75 J. Guo, X. Zhang, Y. Sun, L. Tang and X. Zhang, *J. Mater. Chem. A*, 2017, **5**, 11309–11315.
- 76 J. Zhang, T. Wang, D. Pohl, B. Rellinghaus, R. Dong, S. Liu, X. Zhuang and X. Feng, *Angew. Chem.*, 2016, **128**, 6814–6819.
- 77 J. Zhou, H. Xiao, B. Zhou, F. Huang, S. Zhou, W. Xiao and D. Wang, *Appl. Surf. Sci.*, 2015, **358**, 152–158.
- 78 F. Li, J. Li, Z. Cao, X. Lin, X. Li, Y. Fang, X. An, Y. Fu, J. Jin and R. Li, *J. Mater. Chem. A*, 2015, **3**, 21772–21778.
- 79 X. Qian, J. Ding, J. Zhang, Y. Zhang, Y. Wang, E. Kan, X. Wang and J. Zhu, *Nanoscale*, 2018, **10**, 1766–1773.
- 80 C. Du, H. Huang, X. Feng, S. Wu and W. Song, *J. Mater. Chem. A*, 2015, **3**, 7616–7622.